Sensors & Actuators: A. Physical 393 (2025) 116751

Contents lists available at ScienceDirect

Sensors and Actuators: A. Physical

journal homepage: www.journals.elsevier.com/sensors-and-actuators-a-physical

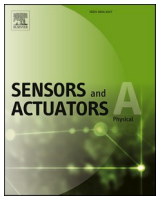

A compact diamagnetic levitation accelerometer with minimized size and high sensitivity

Yuanping Xu [a,*], Zeyu Wang [a], Lu Yang [b], Yang Wang [a], Jin Zhou [a], Hanchao Sun [a], Yongwen Li [a]

[a] College of Mechanical and Electrical Engineering, Nanjing University of Aeronautics and Astronautics, Nanjing 210016, China
[b] College of Civil and Transportation Engineering, Hohai University, Nanjing 210098, China

ARTICLE INFO

Keywords:
Accelerometer
Diamagnetic Levitation
Scaling effect
Minimization

ABSTRACT

Despite the great potential of diamagnetic levitation technology for constructing high sensitivity accelerometer, the development of compact or miniaturized versions remains an ongoing task. Herein, a compact diamagnetic levitation accelerometer with minimized size and high sensitivity is implanted. Specifically, a systematical investigation is conducted to dig out the dynamic response of diamagnetic levitation system consisting of permanent magnet and disk-shaped pyrolytic graphite sheet considering scaling effect. Accompanied by the optimized yet minimized structural parameters of diamagnetic structure, an additional capacitive displacement probe is proposed to detect the axial displacement of pyrolytic graphite sheet. Further experiments validated that the assembled diamagnetic levitation accelerometer is both compact and sensitive, demonstrating an overall size of 12.0 cm^3 and a sensitivity of 0.29 pF/g over a bandwidth of 3.0–6.0 Hz. These characteristics emphasize the versatility and potential of this system, showcasing its applicability as a compact, high-performance accelerometer for practical applications with space demands.

1. Introduction

Diamagnetic levitation refers to a fascinating effect where diamagnetic materials experience a repulsive force from external magnetic field, counteracting gravity and causing thus inducing levitation [1,2]. With the inherent merits of friction-free operation, low magnetic stiffness, structural simplicity and low cost, diamagnetic levitation holds tremendous potential in developing compact, efficient and robust sensors represented by accelerometers [3–7].

Accelerometers are devices highly sensitive to acceleration and vibration [8–10]. By providing superior precision and stability, diamagnetic levitation can significantly improve the accuracy and reliability of accelerometers, making them even more effective in measuring acceleration with unparalleled sensitivity [11]. The earliest foray into integrating diamagnetic levitation into accelerometer designs can be traced to the work of Barrot et al. They proposed a novel design concept for diamagnetic levitation accelerometers that combined staggered cubic permanent magnets, a pyrolytic graphite disk as proof mass and two optical displacement sensors [12]. Further advancements were made by Wang et al. [13], who implanted a novel permanent magnet-diamagnetic hybrid levitation accelerometer coupled with an optical displacement interferometer. By utilizing a levitated permanent magnet rather than pyrolytic graphite as proof mass, the accelerometer was able to reduce magnetic stiffness, yielding an impressive sensitivity of 3.0 mm/g and a residual noise spectrum of 20 ng/$Hz^{1/2}$. Further refinements were demonstrated by Ando et al. [14], who designed a diamagnetic levitation accelerometer using cubic permanent magnets paired with square pyrolytic graphite as proof mass. Their system incorporated an electromagnetic induction coil to capture the radial displacement of the levitated mass, providing both high resolution (0.53 mg) and sensitivity (0.51 mm/g).

Despite the notable and continuous advancements in diamagnetic levitation accelerometers, it is crucial to signify that the development of diamagnetic accelerometers remains in its early stages [15]. The current investigations primarily focused on enhancing the sensitivity of accelerometer by optimizing magnetic field properties of permanent magnets or refining the morphology/mass of proof mass [3,12–14,16,17]. Few efforts have been devoted to exploring compact or miniaturized diamagnetic levitation accelerometers viable for practical applications, particularly in scenarios with stringent space constraints.

In fact, the development of compact or miniaturized versions still remains challenging. One major obstacle is the scaling effect induced by

* Corresponding author.
E-mail address: ypxu@nuaa.edu.cn (Y. Xu).

https://doi.org/10.1016/j.sna.2025.116751
Received 18 March 2025; Received in revised form 24 April 2025; Accepted 28 May 2025
Available online 3 June 2025

the minimized diamagnetic levitation structure. Scaling effect refers to the phenomenon where the characteristics or behavior of system change with size variations. The scaling down of diamagnetic structure that mainly involving in permanent magnet array, would notably affect spatial magnetic field distribution, maximizing the non-uniformity of magnetic field strength [17]. As a result, the induced levitation force instability would cause compromised dynamic response, particularly sensitivity. Another major obstacle lies in the lack of integrated displacement probe compatible with micro diamagnetic structures. The reported diamagnetic levitation accelerometers typically rely on commercial laser displacement probes or laser interferometers for displacement detection [7,11,12]. However, the large size and poor spatial efficiency of these probes make it difficult to integrate them into accelerometers in a compact form. In this regard, exploring efficient, minimized diamagnetic structure and compatible detection probes is urgent for developing compact, miniaturized diamagnetic levitation accelerometers [18,19].

Herein, special attention is focused on implanting minimized diamagnetic levitation structure and compatible displacement detection system. Specifically, a systematical theorical investigation is conducted to dig out the impact of scaling effect on the dynamic response of diamagnetic levitation system consisting of permanent magnet and disk-shaped pyrolytic graphite sheet. Based on the obtained insights, the structural parameters of permanent magnet array are optimized accordingly to pursue the miniaturization of diamagnetic structure while ensuring high sensitivity. Additionally, a capacitive displacement probe based on nested ring electrodes is proposed to complement the minimized diamagnetic structure and detect the axial displacement of pyrolytic graphite sheet. Further experiments validated that the assembled diamagnetic levitation accelerometer is compact yet sensitive, with an overall size of 12.0 $cm^3$and a sensitivity of 0.29 pF/g over a bandwidth of 3.0–6.0 Hz. These characteristics highlight the versatility and potential of this system as viable yet compact diamagnetic levitation accelerometers for practical applications with space demands.

2. Structure and measurement principle of accelerometer

2.1. Structure of accelerometer

The proposed accelerometer is comprised of an array of cylindrical permanent magnets, a disk-shaped pyrolytic graphite sheet, a capacitive displacement probe, and a signal post-processing circuit, as illustrated in Fig. 1(a). To eliminate the adverse effects of mechanical friction on the device, the oscillator of accelerometer is implemented using the diamagnetic levitation structure, as shown in Fig. 1(b). The permanent magnet array, serving as the magnetic source, is composed of a cylindrical permanent magnet and an annular permanent magnet, both axially magnetized and arranged in an "Opposite" configuration. These magnets can bond independently without the need of external assistance, generating a sufficiently strong magnetic field gradient to provide the magnetic stiffness required for the stable levitation of diamagnetic materials. A disk-shaped diamagnetic pyrolytic graphite sheet is levitated above the permanent magnet array, serving as the proof mass of accelerometer. Moreover, considering the levitation characteristics of proof mass, a non-contact displacement measurement probe based on capacitive mechanism is developed, as shown in Fig. 1(c). The capacitive displacement probe comprised of nested electrodes, is mounted on the upper surface of the permanent magnet array, and connected via a coaxial cable to an LC oscillator circuit, which is then linked to a digital capacitance converter (FDC2214). The capacitance output is ultimately read by an STM32 MCU. The basic parameters of each component of the accelerometer are shown in Table 1.

Table 1
Basic parameters of proposed accelerometer.

Parameter	Value
Radius of cylindrical magnet	5 mm
Inner radius of annular magnet	5 mm
Outer radius of annular magnet	10 mm
Height of permanent magnet array	3 mm
Magnetization of annular magnet	7.61×10^5 A/m
Magnetization of cylindrical magnet	-9.35×10^5 A/m
Radius and thickness of pyrolytic graphite sheet	6 mm, 0.5 mm
Magnetic susceptibility of pyrolytic graphite sheet	-310×10^{-6}
Levitated height of pyrolytic graphite sheet	0.65 mm
Radius of capacitive displacement probe's emitting electrode	2 mm
Insulation gap of capacitive displacement probe	0.25 mm
Outer radius of capacitive displacement probe's receiving electrode	4.5 mm
Thickness of the capacitive displacement probe	0.125 mm

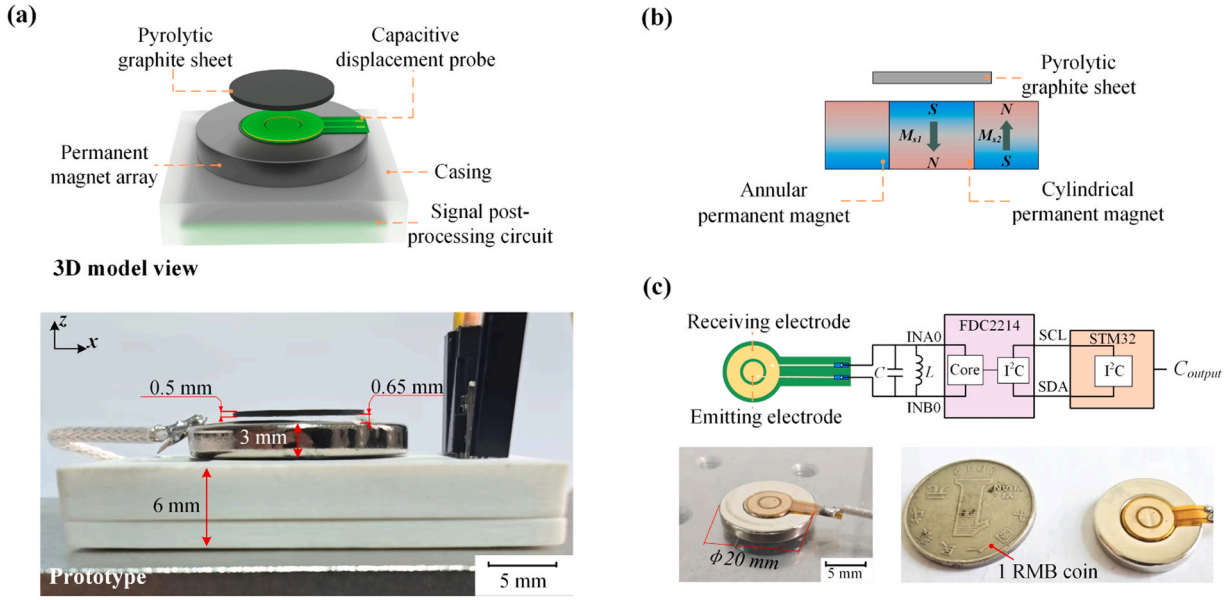

Fig. 1. (a) The structure of the proposed accelerometer (b) oscillator of accelerometer based on diamagnetic levitation (c) capacitive displacement detection system.

2.2. Measurement principle of accelerometer

The measurement principle of accelerometer involves detecting acceleration by measuring the variation in the relative displacement of levitated proof mass. A mechanical analysis is conducted along the measurement axis (z-axis) of device as illustrated in Fig. 2, to establish the dynamic equation of proof mass.

$$m\ddot{x}_z + c\dot{x}_z + kx_z = -mA_{base} \tag{1}$$

Where m represents the mass of the proof mass, x_z, $\dot{x}_z$, $\ddot{x}_z$ denote the displacement, velocity and acceleration of the proof mass along the measurement axis relative to the base, respectively. k is the axial magnetic stiffness coefficient, which is depending on the restoring force provided by the axial diamagnetic force and gravitational force, while c is the axial damping coefficient, equivalently represented by the electromagnetic damping force. A_{base} represents the external excitation acceleration applied to the base.

The dynamic system corresponds to a standard second-order system. After performing the Laplace transform, its transfer function is given by:

$$G(s) = \frac{X_z(s)}{A_{base}(s)} = -\frac{1}{s^2 + \frac{c}{m}s + \omega_n^2} \tag{2}$$

Magnitude-frequency characteristic of the system is given by:

$$A(\omega) = \frac{1}{\omega_n^2\sqrt{\left(1-\frac{\omega}{\omega_n}\right)^2 + \left(2\xi\left(\frac{\omega}{\omega_n}\right)\right)^2}} \approx \frac{1}{\omega_n^2}(\omega << \omega_n) \tag{3}$$

Where ξ represents the damping ratio, and ω_n denotes the natural frequency of the system.

When the base experiences low-frequency vibration along the measurement axis, the proof mass will undergo displacement in the measurement axis direction relative to the base due to the inertial force. Based on the system transfer characteristics described by Eq. (3), the output displacement of proof mass can be mapped to the input acceleration value, enabling the detection of unknown input acceleration. At this point, according to the definition of the sensor's performance parameters, the magnitude of the frequency response can be used to characterize the accelerometer's sensitivity. When the input signal frequency is much smaller than the natural frequency, the amplitude (accelerometer sensitivity) approximates a constant value, which is numerically equal to the inverse of the square of the natural frequency.

Based on the analysis aforementioned, it can be concluded that the natural frequency of diamagnetic levitation system is a key factor influencing the performance of accelerometer, and the natural frequency is negatively correlated with the accelerometer's sensitivity.

2.3. Structure and working principle of capacitive displacement probe

The capacitive displacement detection mainly operates in two modes: self-capacitance and mutual capacitance [20]. Self-capacitance detection features a simple structure and a large sensing range, while mutual capacitance detection offers higher accuracy, superior sensitivity, and does not require the target object to be connected to the circuit directly. In this case, given that the displacement variation is small and it is difficult to connect the levitated graphite sheet with detection circuit directly, mutual capacitance detection mode is employed.

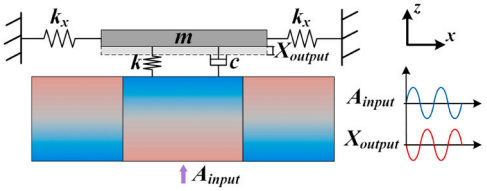

Fig. 2. Mechanical model of the accelerometer.

Mutual capacitance detection is based on the principle of fringe effect of capacitance, which couples with the electric field. Typically, two electrodes are arranged in the same plane, with one acting as the emitting electrode to accumulate charges and generate electric field, while the other serves as the receiving electrode to collect the coupled electric field lines, thus forming a capacitor. When the target object approaches, the coupled electric field lines are altered, which changes the capacitance of the plates. In this design, the probe's electrodes are designated as a nested ring structure: the inner circular electrode acts as the emitting electrode, and the outer ring electrode serves as the receiving electrode, separated by an insulating layer, as shown in Fig. 3 (a). This configuration offers superior linearity compared to a rectangular structure [21]. A flexible PCB is used to fabricate the electrode plates, which reduces the probe's thickness and enhances its stability.

Fig. 3(b) manifests the electric potential and electric field distribution of probe upon the unit excitation applied to emitting electrode. It is evident that the pyrolytic graphite sheet interacts with the electric field lines. As the position of the graphite sheet changes, it alters the distribution of coupled electric field lines, leading to a variation in potential and a corresponding change in the capacitance between the electrodes. In practical applications, the capacitance value will be output through a conversion circuit, enabling the conversion of the displacement signal into an electrical signal.

3. Mathematical modeling of accelerometer

3.1. Modeling of diamagnetic force

First, a mathematical model is established for the magnetic field of permanent magnets, serving as the theoretical foundation for analyzing the spatial magnetic field environment. Based on the equivalent current method [22], the spatial magnetic field model of a single cylindrical permanent magnet is constructed. The magnetic flux density at any observation point in space can be expressed as:

$$B_r(r,\phi,z) = \frac{\mu_0 M_s}{4\pi}\int_{z_1}^{z_2}\int_0^{2\pi}\frac{\cos(\phi-\phi')(z-z')}{|P-P'|^3}r'd\phi'dz' \tag{4}$$

$$B_z(r,\phi,z) = \frac{\mu_0 M_s}{4\pi}\int_{z_1}^{z_2}\int_0^{2\pi}\frac{-(r\cos(\phi-\phi')-r')}{|P-P'|^3}r'd\phi'dz' \tag{5}$$

$$B_\phi(r,\phi,z) = 0 \tag{6}$$

In the above equations, $\mu_0 = 4\pi \times 10^7 N/A^2$ is the vacuum permeability, M_s is the magnetization intensity of the permanent magnet, z_1 and z_2 are the z-axis coordinates of the bottom and top surfaces of permanent magnet, and $|P-P'|$ is the distance from the observation point to the source point, which is expressed as: $(r^2 + r'^2 - 2rr'\cos(\phi-\phi') + (z-z')^2)^{\frac{3}{2}}$

The annular permanent magnet can be equivalently modeled as the Boolean subtraction of two cylindrical permanent magnets with opposite magnetization directions. Therefore, the permanent magnet array used can be equivalently represented as the superposition of three cylindrical permanent magnets, as shown in Fig. 4. The magnetic flux density generated by the permanent magnet array at any point in space is given by:

$$\boldsymbol{B} = \boldsymbol{B}_{M11} + \boldsymbol{B}_{M12} + \boldsymbol{B}_{M2} \tag{7}$$

Where $\boldsymbol{B}_{M11}$, $\boldsymbol{B}_{M12}$, $\boldsymbol{B}_{M2}$ refer to the magnetic flux densities of three cylindrical permanent magnets.

The relative magnetic susceptibility of diamagnetic materials is

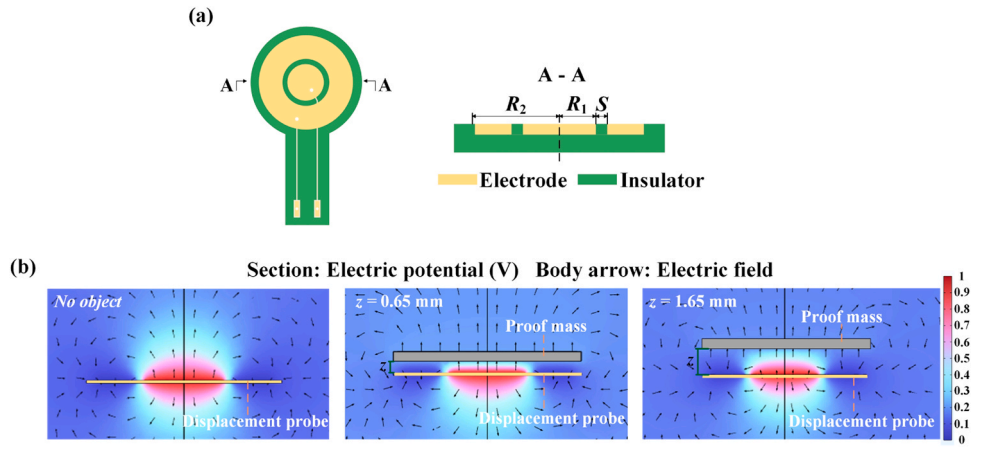

Fig. 3. (a) Structure diagram of capacitive displacement probe (b) simulated electric potential and electric field distribution map of the probe.

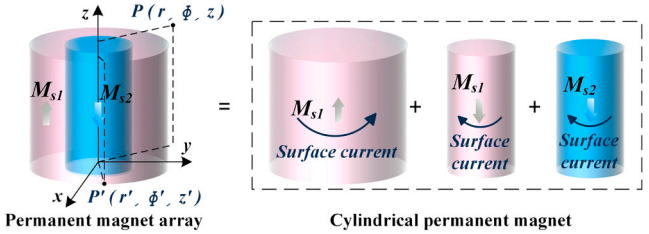

Fig. 4. Equivalent current model of permanent magnet.

negative and relatively small, with a typical order of magnitude of 10^{-5}. In a magnetic field with magnetic flux density $\boldsymbol{B}$, the diamagnetic force acting on a unit volume of diamagnetic material can be expressed as:

$$dF = \boldsymbol{M}_d \cdot (\nabla \cdot \boldsymbol{B}) dv \tag{8}$$

In this expression, $\boldsymbol{M}_d$ represents the induced magnetization of diamagnetic material. When an external magnetic field is applied to pyrolytic graphite, due to its anisotropy, the diamagnetic susceptibility in different directions is not consistent, and it can be expressed as:

$$\boldsymbol{M}_d = \frac{\chi_m}{\mu_0}\boldsymbol{B} = \frac{1}{\mu_0}\begin{bmatrix}\chi_{mr} & 0\\ 0 & \chi_{mz}\end{bmatrix}\cdot\begin{bmatrix}B_r\\ B_z\end{bmatrix} \tag{9}$$

Where χ_{mr} and χ_{mz} represent the radial and axial magnetic susceptibilities of pyrolytic graphite sheet, respectively. By substituting Eq. (9) into Eq. (8), the components of diamagnetic force in each direction are obtained as:

$$F_r = -\frac{\chi_m}{2\mu_0}\iint_S \|\boldsymbol{B}\|^2 \vec{r} \cdot ds \tag{10}$$

$$F_z = -\frac{\chi_m}{2\mu_0}\iint_S \|\boldsymbol{B}\|^2 \vec{z} \cdot ds \tag{11}$$

3.2. Modeling of electromagnetic force

The relative motion between a conductor and a magnetic field induces a change in magnetic flux, generating an induced current and an electromotive force. According to Lenz's law, the conductor experiences an Ampère force that opposes the relative motion. Pyrolytic graphite exhibits good electrical conductivity, with a conductivity of 2.1×10^6 S/m. Therefore, when the pyrolytic graphite sheet undergoes axial vibration, eddy currents are induced on its surface, as shown in Fig. 5, resulting in an electromagnetic damping force that opposes the relative motion.

Since the frequency of the conductor cutting the magnetic field lines is extremely low, the skin effect of eddy currents can be considered negligible, and the eddy currents can be assumed to be uniformly distributed in the thickness direction, so be able to simplify the three-dimensional problem into a two-dimensional one. Since the surface current density $\boldsymbol{K}$ is parallel to the tangent vector of the conductor, it depends only on the normal magnetic flux density $\boldsymbol{B_n}$. Eddy currents are uniformly distributed across the cross-section, and the current density can be expressed as:

$$\boldsymbol{J} = \frac{\boldsymbol{K}}{h} \tag{12}$$

According to the differential form of Ohm's law:

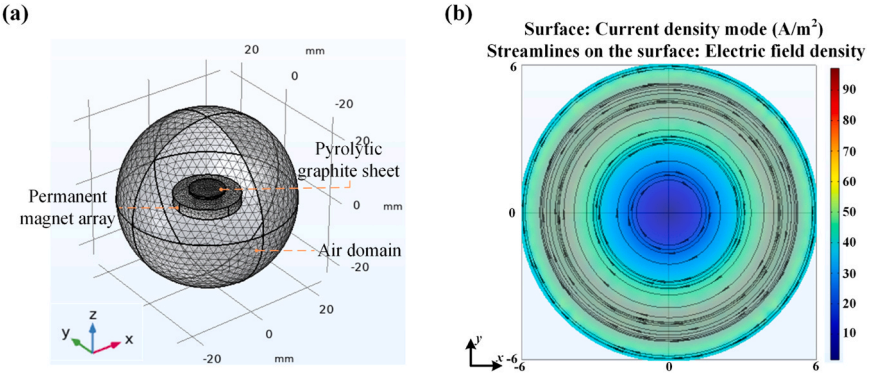

Fig. 5. (a) 3D model built in COMSOL software (b) simulated eddy current on the surface of graphite sheet.

$$\boldsymbol{J} = \sigma(\boldsymbol{E} + \boldsymbol{v} \times \boldsymbol{B}) \tag{13}$$

In this equation, $\boldsymbol{J}$ represents the current density, $\boldsymbol{v}$ is the velocity of the graphite sheet, $\boldsymbol{B}$ is the magnetic flux density, $\boldsymbol{E}$ is the electric field strength, and σ is the electrical conductivity.

For a constant magnetic field, the form of Maxwell's equations is given by:

$$\nabla \times \boldsymbol{E} = -\frac{\partial \boldsymbol{B}}{\mathrm{dt}} = 0 \tag{14}$$

Taking the curl of both sides of Eq. (14) in cylindrical coordinates, the following expression is obtained:

$$\frac{1}{r'}\left[\frac{\partial(r' J_{\theta'})}{\partial \theta'} - \frac{\partial(J_{r'})}{\partial \theta'}\right] = -\sigma\left(v_r \frac{\partial B_z}{\partial r} + v_\theta \frac{\partial B_z}{r \partial \theta} + v_z \frac{\partial B_z}{\partial z}\right) \tag{15}$$

In this equation, $J'_{\theta'}$ and $J'_{r'}$ represent the azimuthal and radial components of current density, respectively. The right-hand side refers to the source term, which is the excitation source of the eddy currents, determined by the motion of graphite sheet and the initial magnetic field distribution.

A scalar potential D' is introduced to describe the surface current density $\boldsymbol{K}'$:

$$K'_{\theta'} = \frac{\partial D'}{\partial r'}, K'_{r'} = -\frac{\partial D'}{r' \partial \theta'} \tag{16}$$

When the excitation source is in the form of axial vibration, Eq. (16) can be written as:

$$\frac{1}{r'}\frac{\partial D'}{\partial r'} + \frac{\partial^2 D'}{\partial r'^2} + \frac{1}{r'^2}\frac{\partial^2 D'}{\partial \theta'^2} = -\sigma h v_z \frac{\partial B_z}{\partial z} \tag{17}$$

The expression for the scalar potential is obtained using the method of images [23]:

$$D|^{Q} = -\frac{h\sigma}{4\pi} v_z \cdot \int_{S_{Q'}} \frac{\partial B_z^0}{\partial z} \ln \sqrt{\frac{R^4 + r_Q^2 r^2 - 2 r_Q r R^2 \cos(\theta_Q - \theta)}{R^2(r_Q^2 + r^2 - 2 r_Q r \cos(\theta_Q - \theta))}} dS_{Q'} \tag{18}$$

The axial electromagnetic force induced by the eddy currents is expressed as:

$$F_z = \iint_{S'} (K'_r B_r + K'_\theta B_r) ds' \tag{19}$$

Where s' is the surface area of graphite sheet. The axial electromagnetic force F_z is directly proportional to the axial velocity v_z, and can be equivalently treated as a damping force with a proportionality coefficient corresponding to the damping coefficient.

3.3. Capacitance modeling of capacitive displacement probe

To investigate the capacitance-displacement relationship of the capacitive displacement probe, Laplace analytical method is used to mathematically model the probe. The geometric model of the probe's cross-section is shown in Fig. 6.

For the space between the electrode surface and the object surface, the space charge density is zero. Therefore, the Laplace equation can be established in cylindrical coordinates as:

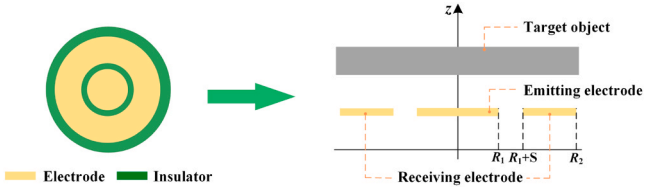

Fig. 6. The geometric model of the probe's cross-section.

$$\frac{\partial^2 V}{\partial r^2} + \frac{1}{r}\frac{\partial V}{\partial r} + \frac{1}{r^2}\frac{\partial^2 V}{\partial \varphi^2} + \frac{\partial^2 V}{\partial z^2} = 0 \tag{20}$$

By using the method of separation of variables to express the potential as a product of functions of z and r, and substituting into Eq. (20), the following equation is obtained:

$$\frac{1}{R(r)}\frac{\partial^2 R}{\partial r^2} + \frac{1}{rR(r)}\frac{\partial R}{\partial r} + \frac{1}{Z(z)}\frac{\partial^2 Z}{\partial z^2} = 0 \tag{21}$$

Solving the differential equation, the expression for the potential is obtained as:

$$V(r,z) = (Az + B)(C \ln r + D) + \sum_{n=1}^{\infty}[A_n I_0(\eta_0 r) + B_n K_0(\eta_0 r)] \cdot [C_n \sin(\eta_0 z) + D_n \cos(\eta_0 z)] \tag{22}$$

In this equation, A_n, B_n, C_n, D_n are undetermined coefficients, and I_n and K_n are the modified Bessel functions.

$$I_n = \left(\frac{x}{2}\right)^n \sum_{k=0}^{\infty} \frac{\left(\frac{x^2}{2}\right)^k}{k!\Gamma(n+k+1)} \tag{23}$$

$$K_n = \left(\frac{\pi}{2}\right)\frac{I_{-n} - I_n}{\sin(n\pi)} \tag{24}$$

By integrating the electric potential gradient in the z-direction on the receiving electrode, the capacitance expression for the ring structure is obtained as:

$$C_f = 4R_1 \varepsilon_0 \varepsilon_r (\rho_1 + \rho_2) \sum_{n=1}^{\infty} \frac{I_1(n\rho_1)}{I_2(n\rho_2)} K_1(n\rho_2)\{I_1(n\rho_2) \cdot K_1[n(\rho_1 + \rho_s)] - I_1[n(\rho_1 + \rho_s)]\} \tag{25}$$

In this equation, $\rho_1 = \frac{\pi R_1}{d}$, $\rho_2 = \frac{\pi R_2}{d}$, $\rho_s = \frac{\pi R_s}{d}$

In practical applications, parasitic capacitance, such as that from the detection circuit and probe wiring, is generated. Therefore, the total capacitance of the probe is:

$$C_{total} = C_f + C_b \tag{26}$$

When the proof mass undergoes displacement, the capacitance of the capacitor plates will change accordingly:

$$\Delta C_f = \frac{4R_1 \varepsilon_0 \varepsilon_r \pi}{\Delta d}\left(R_1 + R_2\right) \sum_{n=1}^{\infty} \frac{I_1\left(n\frac{\pi R_1}{\Delta d}\right)}{I_2\left(n\frac{\pi R_2}{\Delta d}\right)} K_1\left(n\frac{\pi R_2}{\Delta d}\right)\left\{I_1\left(n\frac{\pi R_1}{\Delta d}\right) \cdot K_1\left[n\left(\frac{\pi R_1}{\Delta d} + \frac{\pi S}{\Delta d}\right)\right] - I_1\left[n\left(\frac{\pi R_1}{\Delta d} + \frac{\pi S}{\Delta d}\right)\right]\right\} \tag{27}$$

The analytical model from Eq. (27) makes it difficult to analyze the linear relationship of displacement probe. In this regard, further investigation into the relationship between the change in capacitance and the change in displacement will be required through subsequent simulations and experiments.

4. Design and simulation of accelerometer

4.1. Scaling effect of permanent magnet array

In the diamagnetic levitation system, the forces acting on the levitated component are divided into volumetric forces (gravity) and surface forces (diamagnetic forces). When the size of the diamagnetic levitation system is scaled proportionally, the volumetric force varies with the cube of the size, while the surface force varies with the square of size. As

a result, the effectiveness of diamagnetic force increases as the system is scaled down. This leads to different equilibrium positions for the levitated elements and alters the dynamic response characteristics of system. On the other hand, the presence of the magnetic inclination angle leads to the non-uniformity change of the spatial magnetic flux density when the size of the permanent magnet array changes along different coordinate axes. Therefore, due to the unique nature of the permanent magnet's magnetic field, it is not appropriate to simply consider a proportional scaling scenario for the system. As the magnetic source in the diamagnetic levitation system, the scaling effect mechanism of permanent magnet array should be analyzed first.

Based on the diamagnetic force model aforementioned in Eq. (11), the diamagnetic force along the z axis are affected by three factors, as described in Eq. (28), as follows. From this equation, one can see that in magnetic fields with higher magnetic flux density, a steeper gradient of magnetic flux density can provide a larger diamagnetic force. Therefore, the rate of magnetic field decay is a key qualitative indicator for measuring the strength of diamagnetic force.

$$F_z \propto \chi_{mz} \cdot B_z \cdot \frac{\partial B_z}{\partial z} \tag{28}$$

In a diamagnetic levitation system, the levitated object is typically positioned in the region with the largest magnetic field gradient. The magnetic field gradient along the center axis of permanent magnet can directly reflect the magnetic field variation characteristics in this region, thereby correlating with the diamagnetic force. Considering that the height and radius of the permanent magnet array are responsible for the resultant magnetic field gradient, the effects of varied height and radius on the axial magnetic flux density distribution was firstly investigated using the control variable method.

To permit a sufficient diamagnetic force to counteract gravity, the outer radius of annular permanent magnet is set to be twice the inner radius in this case. The inner radius of the permanent magnet array is maintained at different constants, and the effect of the height parameter of the permanent magnet is considered separately based on the model built in Section 3.1. As shown in Fig. 7, one can observe that when the radius of permanent magnet remains constant, the gradient of the axial magnetic flux density first increases slowly and then almost remains unchanged with increasing height of permanent magnet. Moreover, as the radius of the permanent magnet decreases, the effect of changes in the height of the permanent magnet on the magnetic field's gradient becomes progressively weaker.

The effect of radius parameter on magnetic flux density is also studied with fixed height of permanent magnet. The obtained results are displayed in Fig. 8. Obviously, the gradient of the axial magnetic flux density decreases with increasing radius, and the change amplitude is more significant when compared to the variation caused by height. Moreover, with declined height, the effect of radius on the magnetic field becomes progressively stronger.

Based on the analysis aforementioned, it can be concluded that the height inserts relatively weaker effect on the magnetic field, while the radius can significantly influence the magnetic field. Moreover, the radius is negatively correlated with the axial magnetic field gradient. As diamagnetic force is directly influenced by magnetic field gradient as shown Eq. (28), it can be deduced that the radius would also significantly affect the resultant diamagnetic force.

4.2. Parameter design of diamagnetic levitation structure based on scaling effect

As derived in Section 2.2, when the accelerometer operates within the working frequency range, the sensitivity of accelerometer is negatively correlated with the natural frequency of the diamagnetic levitation structure. This conclusion indicates that a decrease in the natural frequency can effectively enhance the sensitivity of accelerometer. The natural frequency of diamagnetic levitation system is related to the mass of proof mass and the magnetic stiffness, which can be expressed as:

$$\omega_n = \sqrt{\frac{k}{m}} = \sqrt{\frac{\chi_{mz}}{\mu_0} \frac{\partial\left(\int_0^{r_d} B_z^2 \pi r dr\right)}{\partial z}\Big|_{z=z_0}} \tag{29}$$

The analysis presented in Section 4.1 confirms that the size parameters, particularly the radius of permanent magnet array have a significant impact on the spatial magnetic field gradient. Changes in the spatial magnetic field gradient directly affect the system's magnetic stiffness characteristics, thereby altering the system's inherent frequency and sensitivity. Therefore, investigating how the size parameters of permanent magnet array affect the accelerometer sensitivity is crucial for the further parameters' optimization.

In this work, the varied size parameters of permanent magnet array would lead to alterations of static levitation height of proof mass. Therefore, the levitation height z0 should be considered as an additional variable. Meanwhile, the radius of proof mass must be appropriately selected to ensure stable radial levitation. To simplify the calculation process and ensure the stable levitation of the proof mass, the radius of the proof mass is fixed and set to be approximately equal to the inner radius of the permanent magnet plus 1 mm. The selected range of structural parameters for the accelerometer is shown in Table 2:

MATLAB simulation is then used to analyze the relationship between the natural frequency and the varied size parameters based on Eq. (29). The obtained results are shown in Fig. 9. Clearly, one can see that the natural frequency is negatively correlated with the inner radius of permanent magnet array. Specifically, as the radius decreases, the natural frequency would increase up to 25.76 Hz, corresponding to a minimum sensitivity of 0.37 mm/g. The impact of height on the natural frequency is relatively weak. Initially, a down-trend in natural frequency is observed with increasing height, followed by an up-trend with further increasing height. With a height of 5 mm and inner radius of 6 mm, the natural frequency reaches a minimum of 15.07 Hz, corresponding to a sensitivity of 1.09 mm/g. Sensitivity analysis of the input parameters

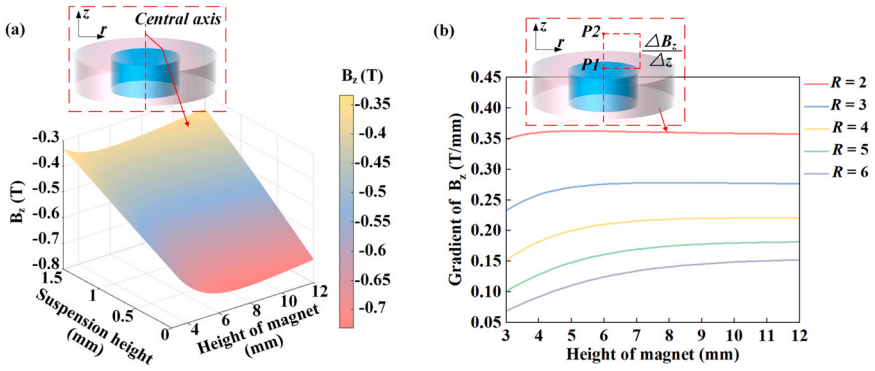

Fig. 7. Study on the height of magnets: (a) axial magnetic flux density (b) the axial gradient of magnetic flux density.

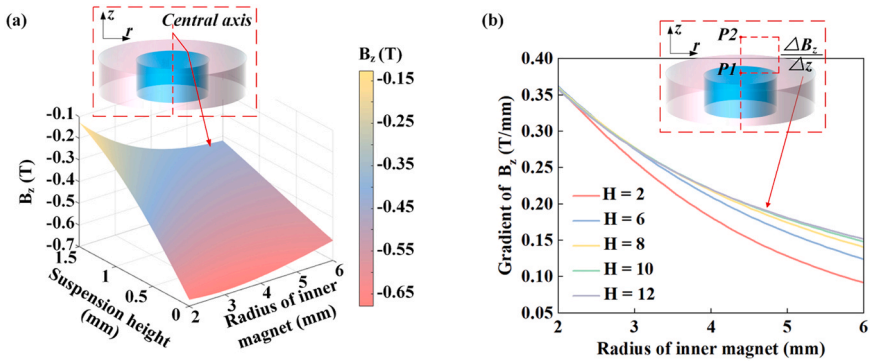

Fig. 8. Study on the radius of magnets: (a) axial magnetic flux density (b) the axial gradient of magnetic flux density.

Table 2
Range of parameters studied.

Symbol	Parameter	Value
R_1	Radius of cylindrical magnet	2–6 mm
R_2	Outer radius of annular magnet	2 R mm
Z	Height of permanent magnet array	3–12 mm
M_{s1}	Magnetization of annular magnet	10×10^5 A/m
M_{s2}	Magnetization of cylindrical magnet	-10×10^5 A/m
r	Radius of pyrolytic graphite sheet	(R+1) mm
h	Thickness of pyrolytic graphite sheet	0.5 mm
X_{mz}	Axial magnetic susceptibility of pyrolytic graphite sheet	-450×10^{-6}
ρ	Density of the pyrolytic graphite sheet	2.25 g/cm^3

using Isight software reveals that the radius and height of the permanent magnet array contribute 92.79 % and 7.21 %, respectively, to the sensitivity of the natural frequency of the diamagnetic levitation oscillator.

From the analysis mentioned above, one can see that the radius of permanent magnet array is the primary factor affecting the natural frequency and consequently sensitivity of diamagnetic levitation system. As the radius of the permanent magnet array increases, the system's natural frequency decreases, and the corresponding accelerometer sensitivity increases. On the other hand, the height of the permanent magnet array has a minimal impact on the accelerometer sensitivity. The overall size of the accelerometer can be reduced by decreasing height without significantly affecting the sensitivity. To enable the high sensitivity along the z axis and meanwhile minimize the global size of accelerometer, the radius parameter and height parameter are optimized, as shown in Table 3.

4.3. Simulation analysis of dynamic characteristics

Based on the optimized size parameters, a further dynamic characteristic analysis is performed to study the performance of accelerometer.

To improve the accuracy of the magnetic field model, surface magnetic field measurements were conducted using the surface magnetic field automatic testing platform (TUNKIA: TD8420) on the plane above the permanent magnet. A set of measured experimental values was used as samples, and the magnetic field model's magnetization intensity of permanent magnet was corrected using a particle swarm optimization algorithm, resulting in $M_{s1} = 7.61 \times 10^5$ A/m and $M_{s2} = -9.35 \times 10^5$ A/m. These parameters were substituted into the mathematical model, and MATLAB was used for calculations. The results were compared with the experimental values, as shown in Fig. 10(a). From Fig. 10(a), it can be observed that the theoretical model values are in good agreement with the experimental values, validating the accuracy of model.

Furthermore, axial diamagnetic force calibration was performed using a precise balance. By adjusting the lifting platform to simulate changes in the suspension height, the readings of balance were recorded to obtain the relationship between the diamagnetic force and the height variation. The axial magnetic susceptibility was corrected to be 310×10^{-6}. The experimental results were compared with the model calculations, as shown in Fig. 10(b), where the theoretical model values closely match the experimental values.

Without vibration signal input, the axial diamagnetic force acting on the proof mass equals to the gravitational force, and the system is in a state of equilibrium along the measurement axis. Based on the force model, the position at which the two forces balance is calculated, and

Table 3
Optimized parameters of accelerometer.

Symbol	Parameter	Value
R_1	Radius of the cylindrical magnet	5 mm
R_2	Outer radius of the annular magnet	10 mm
Z	Height of permanent magnet array	3 mm
r	Radius of the pyrolytic graphite sheet	6 mm
h	Thickness of the pyrolytic graphite sheet	0.5 mm
m	Mass of the pyrolytic graphite sheet	179 mg

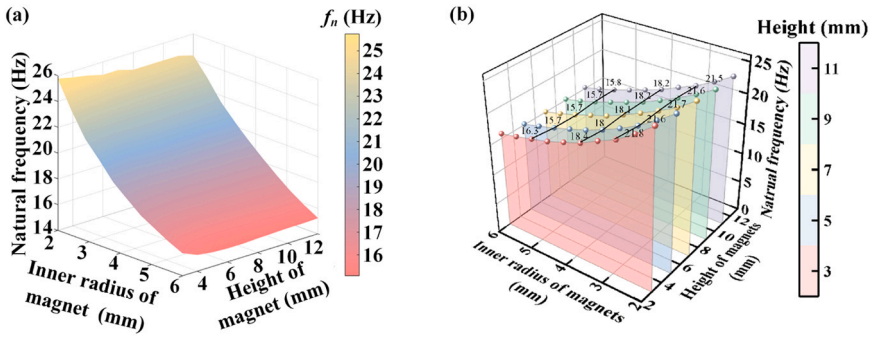

Fig. 9. (a) Natural frequency of diamagnetic levitation structure (b) influencing factors of natural frequency.

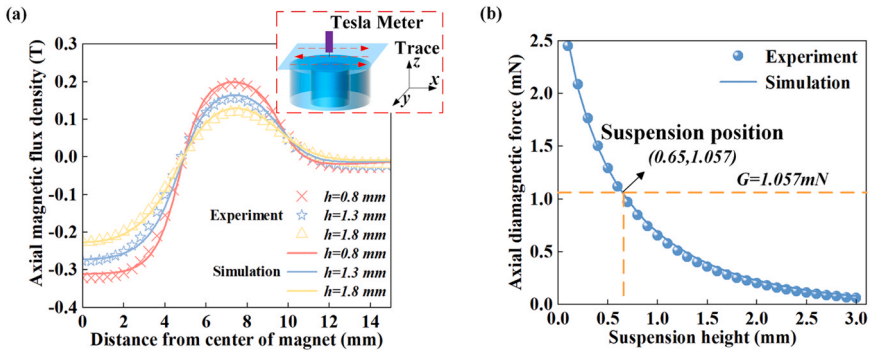

Fig. 10. (a) Axial magnetic flux density of different height surfaces (b) axial diamagnetic force at different height.

the proof mass has a suspension height of 0.65 mm at this point. When a vibration signal is input, the proof mass undergoes axial displacement, and the diamagnetic force generates a restoring force to bring it back to the equilibrium position. In this case, the diamagnetic restoring force can be equivalent to a stiffness effect. Based on the mathematical model of the diamagnetic force, MATLAB simulations are conducted to calculate and fit the relationship curve between the net force acting on the proof mass and the displacement when it deviates from the equilibrium position, as shown in Fig. 11(a). Within the typical working displacement range (± 0.2 mm), the curve exhibits a good linear relationship, and the accelerometer's equivalent magnetic stiffness is linearized to 1.416 N/m.

Similarly, the effect of electromagnetic force can be equivalently treated as a damping effect. Finite element simulation software COMSOL is used to simulate the axial vibration of the pyrolytic graphite sheet, and the curve of equivalent electromagnetic damping versus suspension height is shown in Fig. 11(b). The value of electromagnetic damping decreases as the suspension height increases. In the proposed accelerometer, the change in damping caused by axial vibration micro-displacement during operation is small, and the damping coefficient can be simplified to the equivalent electromagnetic damping at the suspension height, which is 2.13×10^{-3} N/(m/s).

The dynamic characteristics of accelerometer are simulated based on equivalent stiffness and damping. Under sinusoidal excitation, Fig. 12(a) shows the input and output curves of the accelerometer with a 3 Hz sine signal input. It can be observed that the displacement signal and the acceleration signal are proportional and inversely related, in accordance with the amplitude-frequency characteristics described in Eq. (3). Fig. 12(b) presents the frequency response simulation results of the accelerometer, with the first-order resonance peak occurring at 18.19 Hz. To ensure measurement accuracy, the frequency corresponding to an error of less than or equal to 10 % is taken as the working frequency. Therefore, the frequency response range of the accelerometer is 0–5.5 Hz, and the structural sensitivity is 0.75 mm/g.

4.4. Simulation and structure optimization of capacitive displacement probe

As indicated by Eq. (27), the change in capacitance is related to the geometric dimensions of the electrode plates. Considering both the dimensions of the permanent magnet array and the limitations of electrode fabrication, three probes with different size parameters were selected. MATLAB simulations were conducted based on the mathematical model in Section 3.3 to investigate the variation of capacitance with distance for probes of different sizes. The results are shown in Fig. 13(a), among the three selected sizes, when the insulation gap is consistent, a larger electrode area results in higher probe sensitivity; conversely, when the electrode area is fixed, a smaller insulation gap leads to higher probe sensitivity. The probe with dimensions $R_1 = 2$ mm, $S = 0.25$ mm, and $R_2 = 4.5$ mm demonstrates the highest sensitivity, and this electrode is chosen as the probe for the capacitive displacement detection device. Moreover, it is also found that as the gap decreases, the linearity of the probe deteriorates. However, considering the small measurement range, the linearity remains acceptable within a 1 mm detection range. Therefore, the probe configuration with higher sensitivity was chosen.

Then the static calibration of capacitive displacement detection system was carried out. The displacement of proof mass was measured using a Z-axis displacement platform, while the change in the capacitance between the plates was monitored using the post-processing circuit. The results, shown in Fig. 13(b), indicate that the sensitivity of the displacement detection system is 0.3919 pF/mm.

5. Experiment

5.1. Experimental settings

The measurement of the natural frequency of the diamagnetic levitation structure and the calibration experiment of the accelerometer were conducted using the vibration excitation method under Earth's

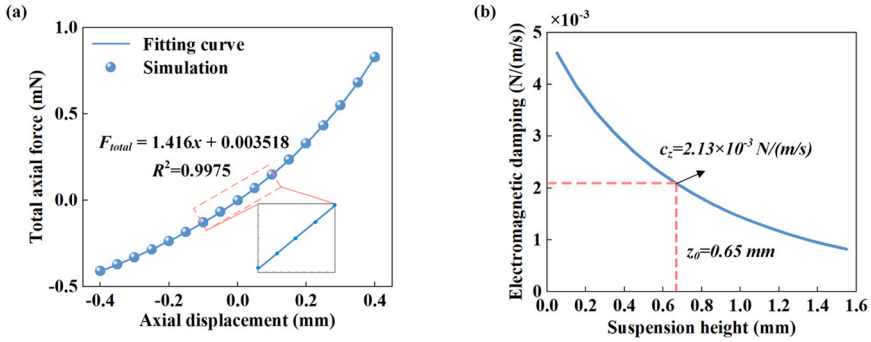

Fig. 11. (a) Equivalent stiffness fitting curve (b) equivalent damping simulation curve.

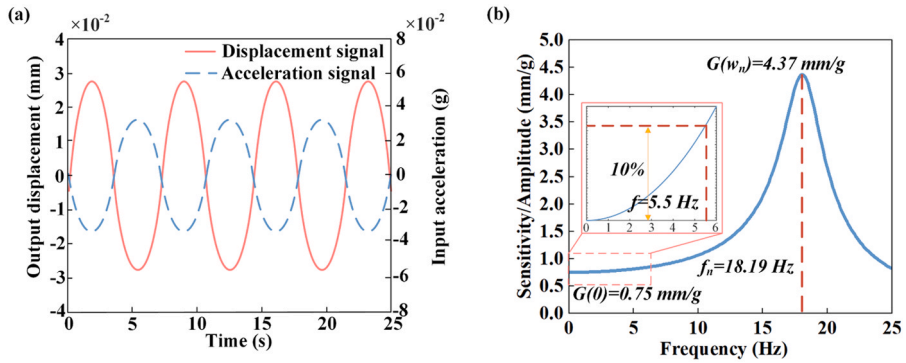

Fig. 12. (a) Input-output response curve of the system under sinusoidal input (b) frequency response curve of accelerometer.

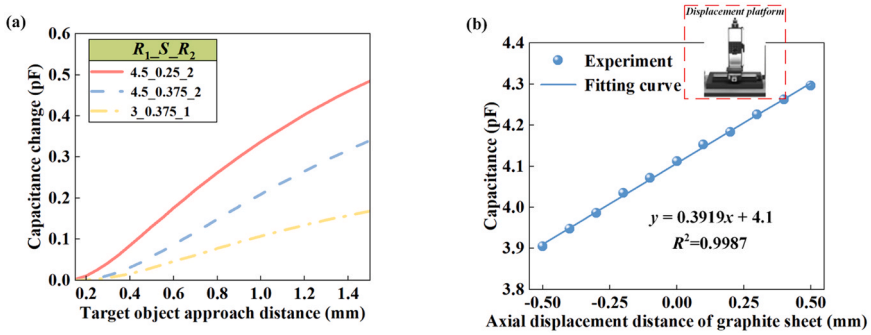

Fig. 13. (a) Variation law of plate capacitance and displacement (b) static calibration curve of capacitive displacement probe.

gravitational field. The experiment utilized a shaker (Sushi DC-300–3) as the vibration source, with the reference input signal being the acceleration value set through its closed-loop controller. Noted that the experiment was conducted at a fixed room temperature (25 ℃) and the effect of temperature fluctuations on the performance of accelerometer can be ignored.

The configuration of experimental setup is shown in Fig. 14. Two accelerometers are attached to the surface of the shaker to measure the real-time deviation between the actual acceleration and the preset acceleration, and this deviation signal is fed back to the controller. The controller then posts an acceleration adjustment command, converting the feedback signal into a voltage signal that is sent to the power amplifier, which drives the actuator to generate desired excitation acceleration.

In the dynamic response verification experiment based on scaling effect, the oscillator's base of diamagnetic levitation accelerometer is fixed onto the shaker to ensure precise linear vibration transmission. The excitation signal is generated using the shaker, and a laser vibrometer is employed to directly measure the displacement output of oscillator.

For the calibration experiment of accelerometer, the laser vibrometer is removed, and the capacitive displacement sensing unit integrated into the designed diamagnetic levitation accelerometer is used for output measurement. The STM32 microcontroller communicates with the displacement-to-capacitance conversion circuit to obtain the capacitive variation of accelerometer output and convert it into acceleration values.

5.2. *Verification of dynamic response characteristic based on scaling effect*

To verify the influence of scaling effect on the dynamic response of accelerometer, five sets of diamagnetic levitation structures with different dimensional parameters were selected for a sinusoidal frequency sweep experiment in the range of 3–30 Hz. The obtained frequency response curves are shown in Fig. 15(a). The dimensional parameters, corresponding natural frequencies, and sensitivities of each experimental group are listed in Table 4.

By comparing the results of Experiments 1–3, it can be observed that

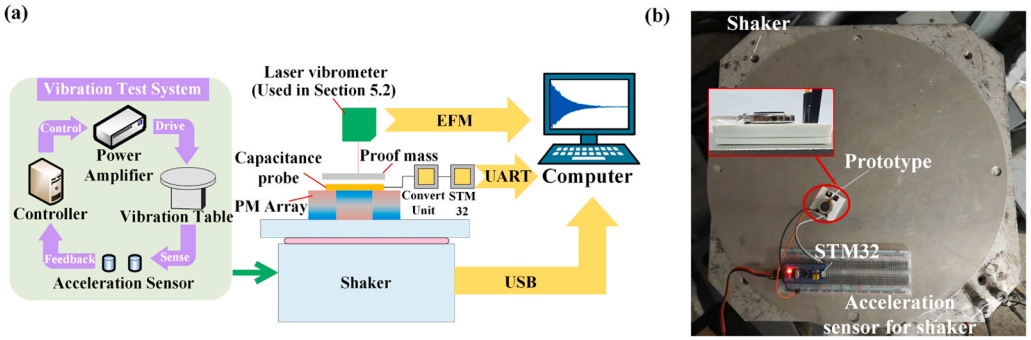

Fig. 14. (a) The configuration of the dynamic excitation measurement (b) experiment setup of calibration.

when the radius of permanent magnet remains constant, the varied height has a minimal effect on the natural frequency and sensitivity. In contrast, from Experiments 3–5, reduced radius significantly declines the sensitivity. The experimental findings are consistent with the simulation results presented in Section 4.2. The results indicate that reducing the height of permanent magnet is of benefit to minimize the overall size while maintaining relatively high sensitivity. However, the radial dimension must be carefully modulated to balance sensitivity and size. Ultimately, the parameters of Group 3 were selected as the final prototype dimensions. And the experimental amplitude-frequency curves of group 3 parameters are consistent with the dynamic simulation results, as shown in Fig. 15(b).

Table 4
Experimental results of prototypes with different sizes.

Group	Height of array	Radius of magnet	Radius of graphite	Natural frequency	Sensitivity
1	10 mm	5 mm	6 mm	18.6 Hz	0.72 mm/g
2	5 mm	5 mm	6 mm	18 Hz	0.77 mm/g
3	3 mm	5 mm	6 mm	18.1 Hz	0.77 mm/g
4	10 mm	2.5 mm	3.5 mm	22 Hz	0.51 mm/g
5	12 mm	4 mm	5 mm	19 Hz	0.70 mm/g

5.3. Accelerometer calibration

The frequency response range of accelerometer refers to the frequency range in which it can accurately detect vibrations, typically defined as the bandwidth where the error does not exceed 10 %. The vibration frequency was increased sequentially from 3 Hz in 1 Hz increments. The identified frequency response range is 3.0 Hz to 6.0 Hz, as shown in Fig. 16(a).

The sensitivity of accelerometer is defined as the ratio of its output to the input acceleration. At a vibration frequency of 3 Hz, the amplitude of shaker was adjusted to change the acceleration magnitude, and the output capacitance values of the accelerometer were recorded. The results, shown in Fig. 16(b), indicate that a linear fit based on the least squares method yields an accelerometer sensitivity of 0.29 pF/g, with a coefficient of determination (R^2) of 0.9985.

At a vibration frequency of 3.0 Hz, the excitation acceleration was gradually reduced until the accelerometer could not output a clearly distinguishable sinusoidal waveform, which defines the resolution of accelerometer. Due to the amplitude limitations of shaker, the measured resolution of accelerometer is better than 3.5 mg, as shown in Fig. 16(b). Nevertheless, it should be noted that the Allan variance curve can also provide valuable insight into the effective resolution of accelerometer. To further clarify the resolution of accelerometer, the Allan variance curve, which calculated from the bias of output (see Fig. 16 (c)), was characterized and illustrated in Fig. 16 (d). Specifically, at an integration time between 0.16 s and 0.33 s, a minimum Allan deviation of 238 μg was observed within an operating bandwidth of 3.0–6.0 Hz. This suggests that the effective resolution of accelerometer is 238 μg.

The linearity of accelerometer is calculated using Eq. (30), resulting in a linearity of 2.25%.

$$e_L = \pm\frac{\Delta max}{y_{FS}} \cdot 100\% = 2.25\% \tag{30}$$

The performances of this minimized accelerometer paper are also compared with the recent work regarding miniature or diamagnetic levitation types. As shown in Table 5, the proposed diamagnetic levitation accelerometer demonstrates a balance between sensitivity and size, highlighting its feasibility for practical applications requiring both sensitivity and constrained spaces, i.e. small-scale robotics, machinery monitoring and portable gravimeter. However, it should be noted that the proposed accelerometer still suffers from the narrow bandwidth limitation. It can only operate within a frequency range of 3.0–6.0 Hz, making it suitable for low-frequency measurements. Further efforts are required to address the narrow bandwidth issue by introducing tunable stiffness strategies.

6. Conclusion

In this work, a compact diamagnetic levitation accelerometer mainly consisting of permanent magnet, disk-shaped pyrolytic graphite sheet and capacitive displacement probe proposed. A systematical investigation is conducted to dig out the dynamic response of diamagnetic structure considering scaling effect. It is found that the height of permanent magnet array has minimal impact on both the central magnetic field distribution and the sensitivity of accelerometer. In contrast, the radius of the permanent magnet is negatively correlated with the central magnetic field gradient, while the sensitivity of the accelerometer is positively correlated with this gradient. Based on this scaling effect mechanism, the structural parameters of accelerometer are optimized yet minimized. Also, an additional capacitive displacement probe based on nested ring electrodes is proposed to detect the axial displacement of pyrolytic graphite sheet. The subsequently assembled diamagnetic levitation accelerometer demonstrated an overall size of 12.0 cm^3 and a sensitivity of 0.29 pF/g over a bandwidth of 3.0–6.0 Hz, highlighting its applicability as compact, high-performance accelerometer for practical applications.

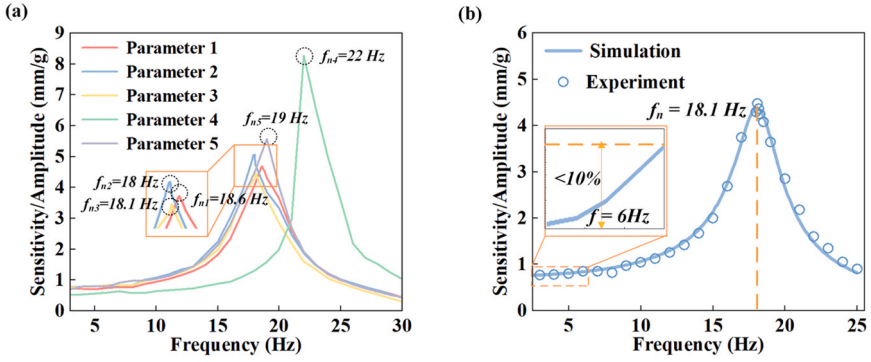

Fig. 15. (a) Results of the sweep frequency experiment (b) comparison between experiment and simulation.

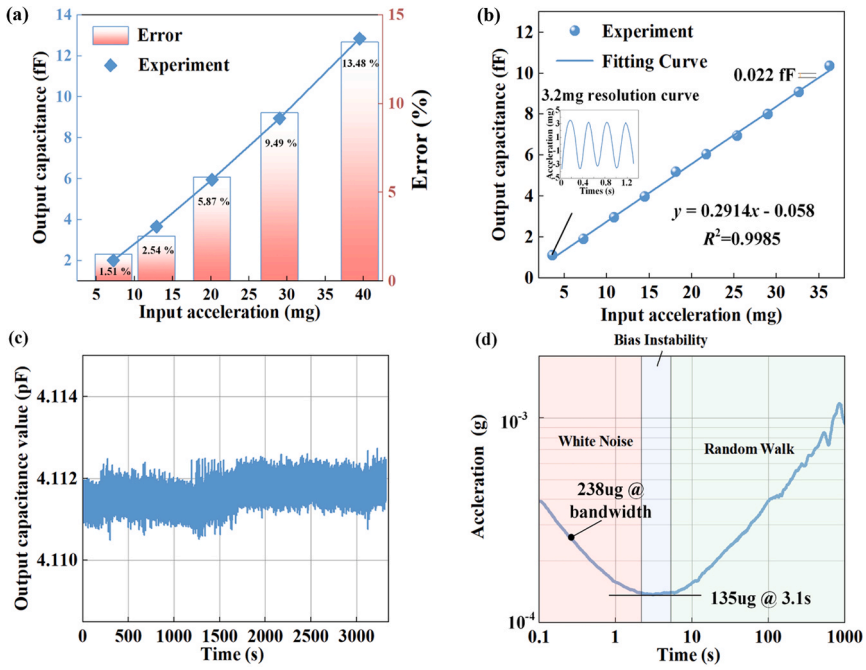

Fig. 16. (a) The frequency range, (b) Input-output response curve, (c) bias of output, (d) allan variance curve of accelerometer.

Table 5
The sensitivity and size of reported minimized accelerometers.

Group	Type	Structural sensitivity	Sensitivity	Size
Ref [13]	Diamagnetic and Permanent magnetic Hybrid Levitation	3 mm/g	3 mm/g	16 cm^3(including oscillator without displacement probe)
Ref [14]	Diamagnetic Levitation with Inductive Probe	0.51 mm/g	12 V/g	19.2 cm^3
Ref [24]	MEMS accelerometer	/	1.01 fF/g	1.44 mm^3 (only including sensing probe)
This work	Diamagnetic Levitation with Capacitive Probe	0.77 mm/g	0.29 pF/g	12 cm^3

Declaration of Competing Interest

We declare that we have no financial and personal relationships with other people or organizations that can inappropriately influence our work, there is no professional or other personal interest of any nature or kind in any product, service and/or company that could be construed as influencing the position presented in, or the review of, the manuscript entitled "**A compact diamagnetic levitation accelerometer with minimized size and high sensitivity**".

Acknowledgements

This work was supported in part by the National Natural Science Foundation of China (Grant Numbers 52275537). The authors would like to thank the staff at Magnetic Levitation and Vibration Control lab (MLVC) at Nanjing University of Aeronautics and Astronautics for technical support.

Data Availability

Data will be made available on request.

References

[1] Y. Xu, Y. Zhang, J. Zhou, C. Jin, Modeling and validation of diamagnetic rotor levitated by permanent magnetics, Chin. J. Mech. Eng. Eng. 37 (2024) 67, https://doi.org/10.1186/s10033-024-01053-1.
[2] J.-Y. Chen, J.-B. Zhou, G. Meng, Diamagnetic bearings for MEMS: performance and stability analysis, Mech. Res. Commun. 35 (2008) 546–552, https://doi.org/10.1016/j.mechrescom.2008.06.008.
[3] Q. Gao, H. Yan, H. Zou, W. Li, Z. Peng, G. Meng, W. Zhang, Magnetic levitation using diamagnetism: mechanism, applications and prospects, Sci. China Technol. Sci. Sci. 64 (2021) 44–58, https://doi.org/10.1007/s11431-020-1550-1.
[4] J. Abadie, E. Piat, S. Oster, M. Boukallel, Modeling and experimentation of a passive low frequency nanoforce sensor based on diamagnetic levitation, Sens. Actuators A Phys. 173 (2012) 227–237, https://doi.org/10.1016/j.sna.2011.09.025.
[5] François Barrot, Acceleration and inclination sensors based on magnetic levitation: application in the particular case of structural health monitoring in civil engineering, No. 4044. EPFL, 2008. https://doi.org/10.5075/epfl-thesis-4044.
[6] G. Aydemir, A. Kosar, H. Uvet, Design and implementation of a passive micro flow sensor based on diamagnetic levitation, Sens. Actuators A Phys. 300 (2019) 111621, https://doi.org/10.1016/j.sna.2019.111621.
[7] Y. Xu, Q. Jiang, K. Yang, J. Zhou, Q. Guo, A novel ultra-high-resolution inclination sensor based on diamagnetic levitation, Sens. Actuators A Phys. 343 (2022) 113686, https://doi.org/10.1016/j.sna.2022.113686.
[8] S. Bruinsma, D. Tamagnan, R. Biancale, Atmospheric densities derived from CHAMP/STAR accelerometer observations, Planet. Space Sci. 52 (2004) 297–312, https://doi.org/10.1016/j.pss.2003.11.004.
[9] M. Rodrigues, B. Foulon, F. Liorzou, P. Touboul, Flight experience on CHAMP and GRACE with ultra-sensitive accelerometers and return for LISA, Class. Quantum Gravity 20 (2003) S291, https://doi.org/10.1088/0264-9381/20/10/332.
[10] Z.-D. Xu, Z. Wu, Energy damage detection strategy based on acceleration responses for long-span bridge structures, Eng. Struct. 29 (2007) 609–617, https://doi.org/10.1016/j.engstruct.2006.06.004.
[11] X. Chen, S.K. Ammu, K. Masania, P.G. Steeneken, F. Alijani, Diamagnetic composites for High-Q levitating resonators, Adv. Sci. 9 (2022) 2203619, https://doi.org/10.1002/advs.202203619.
[12] F. Barrot, J. Sandtner, H. Bleuler, Acceleration sensor based on diamagnetic levitation, in: H. Ulbrich, W. GÜnthner (Eds.), IUTAM Symposium on Vibration Control of Nonlinear Mechanisms and Structures, Springer-Verlag, Berlin/Heidelberg, 2005, pp. 81–90, https://doi.org/10.1007/1-4020-4161-6_6.
[13] Q. Wang, X. Ren, S. Jiao, X. Lei, S. Zhang, H. Liu, P. Luo, L. Tu, A diamagnetic levitation based inertial sensor for geophysical application, Sens. Actuators A Phys. 312 (2020) 112122, https://doi.org/10.1016/j.sna.2020.112122.
[14] B. Ando, S. Baglio, V. Marletta, A. Valastro, A. Pistorio, C. Trigona, A friction less accelerometer exploiting a magnetic levitating mechanism and an inductive readout strategy, in: 2017 IEEE International Instrumentation and Measurement

Technology Conference (I2MTC), IEEE, Torino, Italy, 2017, pp. 1–5. https://doi.org/10.1109/I2MTC.2017.7969961.
[15] G. De Pasquale, S. Iamoni, A. Somà, 3D numerical modeling and experimental validation of diamagnetic levitating suspension in the static field, Int. J. Mech. Sci. 68 (2013) 56–66, https://doi.org/10.1016/j.ijmecsci.2012.12.018.
[16] Y. Wang, Y. Xu, L. Yang, J. Zhou, J. Mahfoud, C. Jin, An ultra-sensitive diamagnetic levitation accelerometer with quasi-zero-stiffness structure, Measurement 245 (2025) 116651, https://doi.org/10.1016/j.measurement.2025.116651.
[17] Ch Pigot, B. Delinchant, G. Poulin, G. Reyne, Optimization of a 3D micro-accelerometer based on diamagnetic levitation, Int. J. Appl. Electromagn. Mech. 30 (2009) 179–188, https://doi.org/10.3233/JAE-2009-1020.
[18] Y. Leng, Y. Chen, R. Li, L. Wang, H. Wang, L. Wang, H. Xie, C.-K. Duan, P. Huang, J. Du, Measurement of the earth tides with a diamagnetic-levitated micro-oscillator at room temperature, Phys. Rev. Lett. 132 (2024) 123601, https://doi.org/10.1103/PhysRevLett.132.123601.
[19] F. Han, B. Sun, L. Li, Q. Wu, Performance of a sensitive micromachined accelerometer with an electrostatically suspended proof mass, Sens. J. IEEE 15 (2015) 209–217, https://doi.org/10.1109/JSEN.2014.2340862.
[20] Y. Ye, C. Zhang, C. He, X. Wang, J. Huang, J. Deng, A review on applications of capacitive displacement sensing for capacitive proximity sensor, IEEE Access 8 (2020) 45325–45342, https://doi.org/10.1109/ACCESS.2020.2977716.
[21] Z. Chen, R.C. Luo, Design and implementation of capacitive proximity sensor using microelectromechanical systems technology, IEEE Trans. Ind. Electron. 45 (1998) 886–894, https://doi.org/10.1109/41.735332.
[22] E.P. FURLANI, Permanent magnet and electromechanical devices, Academic Press, San Diego, 2001, pp. 131–144.
[23] Jie-Yu Chen, Jian-Bin Zhou, Guang Meng, Wen-Ming Zhang, Evaluation of Eddy-Current effects on diamagnetic bearings for microsystems, IEEE Trans. Ind. Electron. 56 (2009) 964–972, https://doi.org/10.1109/TIE.2008.2011346.
[24] T. Tsuchiya, H. Hamaguchi, K. Sugano, O. Tabata, Design and fabrication of a differential capacitive three-axis SOI accelerometer using vertical comb electrodes, IEEJ Trans. Electr. Electron. Eng. 4 (2009) 345–351, https://doi.org/10.1002/tee.20416.

Yuanping Xu received his Ph.D. degree in mechanical engineering from Nanjing University of Aeronautics and Astronautics (NUAA) in 2018. From 2016–2017, He was a guest Ph.D. student in Ecole Polytechnique Federale Lausanne (EPFL), Switzerland. He is currently a associate professor in the college of mechanical and electrical engineering, NUAA. His research focuses on high-performance magnetic levitation systems and manufacturing.

Zeyu Wang is Master student at the College of Mechanical and Electrical Engineering in Nanjing University of Aeronautics and Astronautics. His research is focused on diamagnetic levitation accelerometer.

Lu Yang received the Ph.D degree from Nanjing University of Aeronautics and Astronautics in 2017. She is now an associate professor at the College of Civil and Transportation Engineering in Hohai University. Her research is focused on the fabrication and design of force sensors.

Yang Wang is Ph.D student at the College of Mechanical and Electrical Engineering in Nanjing University of Aeronautics and Astronautics. His research focuses on diamagnetic levitation technology.

Jin Zhou received her Ph.D. degree in mechanical engineering from China University of Mining and Technology (CUMT) in 2001. From 2012–2013, she was a visiting scholar in the rotating machinery and control laboratory (ROMAC) of the University of Virginia. She is currently a full professor in the college of mechanical and electrical engineering, NUAA. Her research focuses on magnetic bearings and vibration control. She was the member of Program Committee of the 14th International Symposium on Magnetic Bearings (ISMB, 2014), the Program Chair of the 16th International Symposium on Magnetic Bearings (ISMB, 2018). she was an elected member of International Advisory Committee of ISMB in 2018.

Hanchao Sun is Master student at the College of Mechanical and Electrical Engineering in Nanjing University of Aeronautics and Astronautics. His research is focused on diamagnetic levitation sensor.

Yongwen Li is Master student at the College of Mechanical and Electrical Engineering in Nanjing University of Aeronautics and Astronautics. His research is focused on diamagnetic levitation technology.